All-optical generation and time-resolved polarimetry
of magneto-acoustic resonances via Transient Grating spectroscopy
- Supplemental Material -

P. Carrara,[1,2] M. Brioschi,[1,2] E. Longo,[3] D. Dagur,[1,4] V. Polewczyk,[1] G. Vinai,[1]

R. Mantovan,[3] M. Fanciulli,[5] G. Rossi,[2] G. Panaccione,[1] and R. Cucini[1]

[1]*Istituto Officina dei Materiali (IOM),*

Consiglio Nazionale delle Ricerche (CNR),

Area Science Park, I-34149 Trieste, Italy

[2]*Dipartimento di Fisica, Università degli Studi di Milano, Via Celoria 16, 20133 Milano, Italy*

[3]*Institute for Microelectronics and Microsystems,*

CNR-IMM Unit of Agrate Brianza, Via C. Olivetti 2, 20864, Agrate Brianza, Italy

[4]*Dipartimento di Fisica, Università degli Studi di Trieste, Via Valerio 2, 34127 Trieste, Italy*

[5]*Dipartimento di Scienza dei Materiali,*

Università degli Studi di Milano Bicocca, Milano IT-20125, Italy

I. SAMPLES CHARACTERIZATION

Here we present Grazing Incidence X-Ray Diffraction (GIXRD) and X-Ray Reflectivity (XRR) measurements performed on samples $SiO_2/Ni(14\ nm)/SiO_2$ and $SiO_2/Ni(14\ nm)/CaF_2$ (we use the convention capping/overlayer/substrate to indicate the sample). Overall, the different crystallization as observed by GIXRD in the two samples, together with their different morphology as observed by XRR, can be correlated to the different results obtained by SAW-FMR in terms of different M_{eff} values, this latter parameter being influenced by the overall magneto-structural properties of the ferromagnetic compound.

A. GIXRD

GIXRD patterns are acquired using a position sensitive gas detector (Inel CPS-120) and a Cu K_α X-ray emission ($\lambda = 1.54178$ Å). In all the measurements, the angle of incidence between the X-ray beam and the sample is fixed at $\omega = 0.5°$. In Fig.S1 the GIXRD patterns for samples $SiO_2/Ni(14$ nm)/SiO_2 (black solid line) and $SiO_2/Ni(14\ nm)/CaF_2$ (red solid line) are reported, for 2θ in the range $95° - 110°$. By comparing the row data with the tabulated diffraction pattern for the Ni powder (database code ICSD 76667), the peaks around $93°$ and $103°$ are assigned to the (311) and (222) reflections, respectively. We extract the size of the Ni crystalline grains by using the Scherrer formula $D = \frac{K\lambda}{B\cos\theta}$, where K is the Scherrer constant fixed at 0.94 for spherical crystallites with cubic symmetry, λ is the X-ray wavelength, B the full width at half maximum of the peak and θ the position of the peak. As a result, D turns out to be 4.4 nm for both films. Despite the latter finding, the higher intensity of the Ni (222) diffraction peak for the $SiO_2/Ni(14\ nm)/CaF_2$ sample indicates a structural configuration different from $SiO_2/Ni(14\ nm)/SiO_2$, the former being characterized by a more pronounced texturization of its crystalline grains.
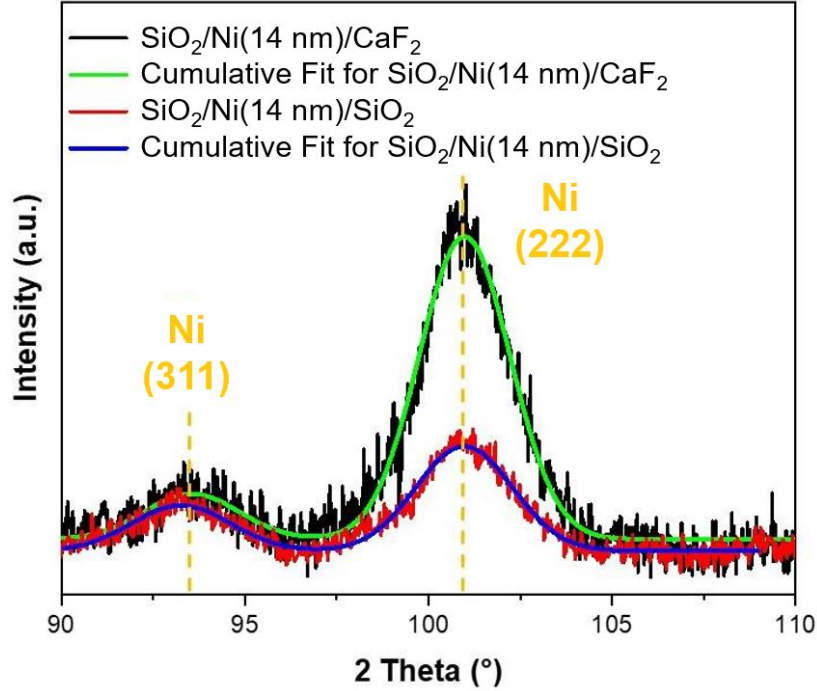
Figure S1. GIXRD patterns for $SiO_2/Ni(14\ nm)/SiO_2$ and $SiO_2/Ni(14\ nm)/CaF_2$, indicated with black and red solid lines, respectively. The green and blue solid lines represent the cumulative fit of the peaks according to a Gaussian distribution.

B. XRR

XRR measurements are conducted using a commercial scintillator. The collected data are simulated according to a matrix formalism model corrected by a Croce-Nevot factor, allowing for the determination of thickness, roughness, and electronic density (ρ_e) for each layer composing the stack. For the Cu K_α emission (1.5406 Å), ρ_e is obtained converting the wave vector transfer q_c extracted from the dataset as q_c (Å^{-1}) $= 0.0375\sqrt{\rho_e\ (e^-/\text{Å}^3)}$. In Fig.S2 the XRR collected spectra (black squares) for the samples $SiO_2/Ni(14\ nm)/SiO_2$ and $SiO_2/Ni(14\ nm)/CaF_2$ are reported; the red solid lines indicate the best fit for the curves. The parameters extracted from the fits in Fig.S2 are summarized in Tab.S1 and Tab.S2. The thickness of each layer is compatible with the nominal value, as well as ρ_e, demonstrating the reliability of the investigated systems from the structural and chemical point of view. The values of the roughness for the Ni layers are strongly influenced by the

adopted substrate: in the case of SiO_2 substrate, the Ni roughness is more than three times larger than for CaF_2 substrate, indicating that the Ni layer is morphologically more ordered on the latter substrate.
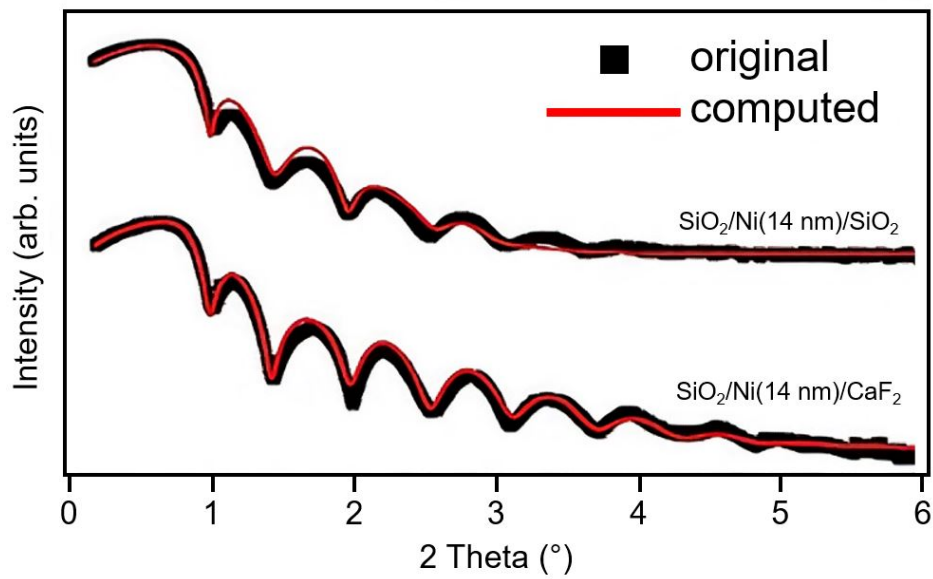

Figure S2. XRR data acquired for samples SiO_2/Ni(14 nm)/SiO_2 and SiO_2/Ni(14 nm)/CaF_2 (black squares). The red solid lines indicate the best fit of the collected dataset.

Table S1. Parameters extracted from the XRR fit of the SiO_2/Ni(14 nm)/SiO_2 dataset.

Layer	Thickness (nm)	ρ_e (e^-/Å^3) measured/nominal	Roughness (nm)
SiO_2	9.6	0.67/0.67	1.3
Ni	14.4	2.38/2.29	1.3
SiO_2	Inf.	0.67 (fixed)	0.9

Table S2. Parameters extracted from the XRR fit of the SiO_2/Ni(14 nm)/CaF_2 dataset.

Layer	Thickness (nm)	ρ_e (e^-/Å^3) measured/nominal	Roughness (nm)
SiO_2	8.5	0.67/0.67	1.2
Ni	14.4	2.30/2.29	0.4
CaF_2	Inf.	0.95 (fixed)	0.7

II. ABSENCE OF IN-PLANE ANISOTROPY FOR FMR MEASUREMENTS

The MOKE characterization of Ni(14 nm)/CaF$_2$ (Fig.2a in the main text) shows a small in-plane magnetic anisotropy in the magnetic remanence. In this section we show that such anisotropy is negligible in the framework of our FMR analysis.

Fig.S3 shows FMR results obtained from the Ni(14 nm)/CaF$_2$ sample with the external magnetic field oriented along two inequivalent axes of the cubic substrate, namely [100] (corresponding to $\varphi = 0°$ with respect to setup scheme in Fig.1 in the main text) and [110] ($\varphi = 45°$); the SAW-FMR data presented in the main text (acquired with $\varphi \approx 15°$) are also reported. Tab.S3 shows the value of M_{eff} and γ obtained by fitting the three datasets with the Kittel formula (Eq.2 in the main text). We obtain largely compatible values of M_{eff}, so we conclude that the anisotropy of the crystalline substrate does not induce a magnetic anisotropy in the Ni film on top observable in FMR measurements. At intermediate φ, spanning from [100] to [110], an even lower dependence of M_{eff} on φ is expected: this legitimates the analysis of FMR and SAW-FMR data with an isotropic Kittel relation.

Table S3. Fit parameters of the data acquired by standard FMR acquired with the external magnetic field along the [100] and [110] crystallographic directions and the SAW-FMR data acquired with the external field at an angle $\varphi \approx 15°$ with respect to [100].

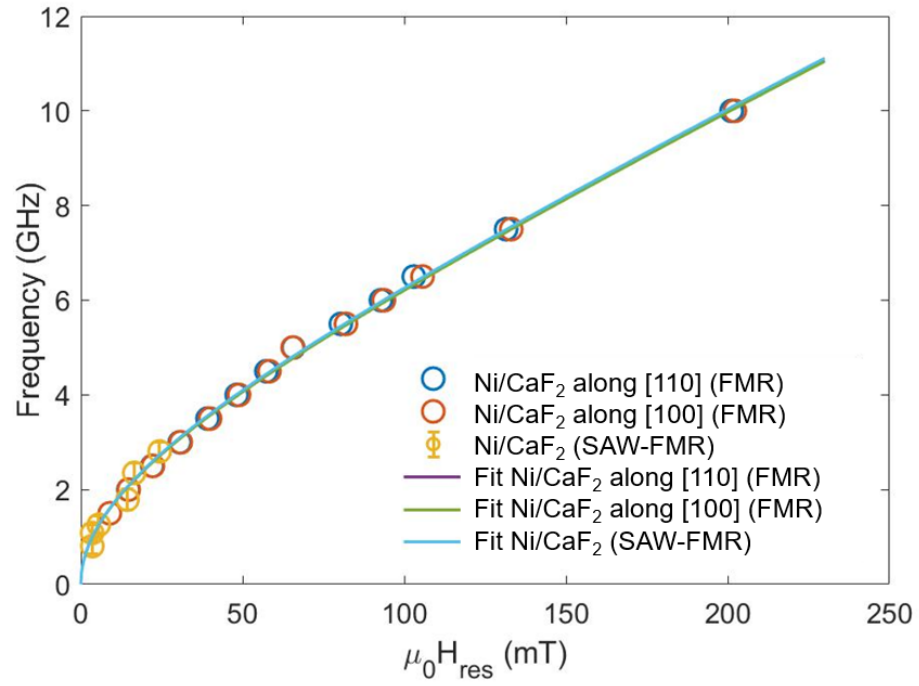| Dataset	M_{eff} (kA/m)	γ (rad/s $\cdot$ T)
FMR along [100]	195 ± 16	$(2.10 \pm 0.06) \cdot 10^{11}$
FMR along [110]	196 ± 17	$(2.10 \pm 0.06) \cdot 10^{11}$
SAW-FMR	199 ± 18	fixed at $2.10 \cdot 10^{11}$

Figure S3. FMR and SAW-FMR data acquired along different crystallographic directions. Blue and orange empty dots are data extracted from standard FMR measurements respectively along the [110] and [100] crystallographic axis, while the yellow ones are the data extracted from SAW-FMR measurements presented in the main text. Solid lines represent the fit of the three datasets.

III.   RAW DATA AND BACKGROUND REMOVAL

A.   Acoustic traces

In Fig.S4 we report the raw data of the acoustic Transient Grating (TG) trace shown in Fig.3 of the main text, together with the fitting function for background removal. Details on the sample and on the experimental conditions can be found in the main text. Blue dots are the raw data included in the fitting. Green diamonds are data excluded from the fitting: indeed, the so-called coherent peak (*i.e.* the intense signal peak due to fast electronic response of the material in the first ps after the TG excitation) severely affects the acquired signal of the first few points after time zero. This is due to the small bandwidth of the photoreceiver and to lock-in amplification, resulting in long integration time and undersampling of the true signal in these acquisitions. A meaningful investigation of the early time region requires finer time steps, and it is beyond the scope of our investigation.

We removed a background (red line) with functional form

$$y_{\text{bkg}} = A \cdot e^{-t/\tau} + m \cdot t + q \,, \tag{S1}$$

for which we obtained $\tau = 372 \pm 60$ ps. The residuals are plotted as light-blue dots: these are the data shown in Fig.3 of the main text. We interpret the linear background for late time delay as a different emerging heat dissipation channel.

B.   Faraday Rotation (FR) traces

We employed the same procedure explained in the previous section. In Fig.S5 two FR traces are shown, for external magnetic field $H_{\text{ext}} = 5.4$ mT and 23.3 mT, corresponding to peak resonance condition for RSAW and SSLW, respectively. Blue dots are the raw data included in the fit; green diamonds are excluded data (see previous section for discussion); red line is the best fit for Eq.S1; light-blue dots are the residuals. Note, with respect to Fig.S4, that the linear background at late time delays is significantly flatter; moreover, the pre-edge data lie on a non-zero baseline, which is due to non complete extinction of the polarizer in the detection branch (acoustic TG is a background-free technique, differently from FR).
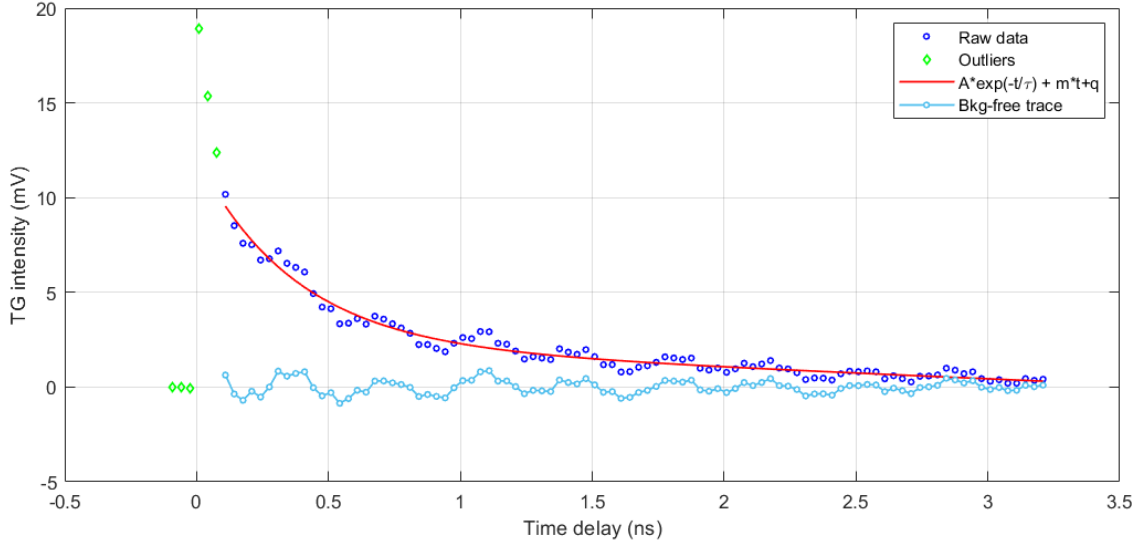
Figure S4. Raw data and background removal for TG acoustic trace. The residuals show oscillations at two frequencies (see main text for details).
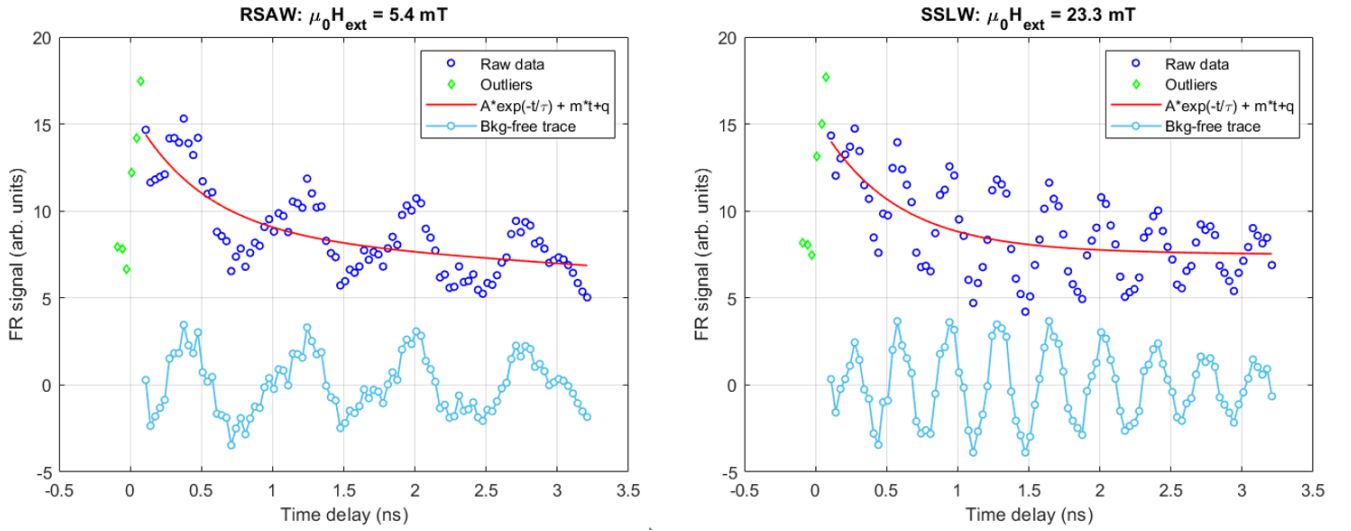

Figure S5. Raw data and background removal from FR traces. Left: RSAW-driven magnetization oscillations. Right: SSLW-driven magnetization oscillations.

9

IV. THERMO-ELASTIC EFFICIENCY

In [12] (pp.84-90), the coupling of thermal and stress-strain gratings is discussed. For amorphous systems (or cubic ones, for wavevector $\boldsymbol{q}$ along $\langle 100 \rangle$), the longitudinal strain u_{xx} along the grating wavevector direction (assumed as the x axis) can be evaluated as

$$u_{xx} = \beta_{\text{eff}} \, \delta T \, , \tag{S2}$$

where δT is the temperature rise inside the medium, and

$$\beta_{\text{eff}} = \alpha_{\text{th}} \left(1 + 2 \frac{c_{12}}{c_{11}} \right) \, ; \tag{S3}$$

α_{th} is the thermal expansion coefficient and c_{ij} are the elastic stiffness coefficients. The ratio c_{12}/c_{11} can be recast using the Poisson ratio ν:

$$\nu = \frac{c_{12}}{c_{11} + c_{12}} \, , \tag{S4}$$

from which

$$\beta_{\text{eff}} = \alpha_{\text{th}} \frac{1 + \nu}{1 - \nu} \, . \tag{S5}$$

On the other hand,

$$\delta T = \frac{Q}{V \, c_{\text{th}}} \, , \tag{S6}$$

where Q is the heat transfer, V is the volume involved in the expansion, and c_{th} is the specific heat capacity at constant pressure.

Thus, for the seek of comparison between different substrates, we can usefully define a thermo-elastic efficiency η as

$$\eta = \frac{u_{xx}}{Q/V} = \alpha_{\text{th}} \frac{1 + \nu}{1 - \nu} \frac{1}{c_{\text{th}}} \, . \tag{S7}$$

The validity of this expression is limited by two assumptions:

- The heat transfer Q is independent on the substrate material under study. This is the case in our experiment, where the absorption of radiative energy from the pump laser mostly takes place in the Ni overlayer, with almost no contribution from the transparent substrate. Thus we can assume that the thermal input stress is the same, for fixed Ni film thickness;

10

- The substrate volume involved in the expansion is independent on the material under study. This assumption is not completely valid in our case, since the volume involved in SAW oscillation depends on the particular acoustic mode considered and on the material, at fixed wavevector. Moreover, we are neglecting heat diffusion phenomena: for example, the amount of volume of substrate involved in thermal expansion depends on thermal conductivity, on thermal contact resistance and on time.

Further investigation could lead to more precise expressions; nonetheless, we believe that Eq.S7 can be a good estimate of the thermo-elastic efficiency in our experiment.

V. SPIN-WAVE DISPERSION

We analyzed the SAW-FMR data on the basis of the Kittel theory, which is derived for uniform precession experiments. A validation of our analysis procedure is presented here, by computation of the SW dispersion. We followed [53], where an approximate analytical relation for dipole-exchange SWs is calculated. The computation uses the following parameters, suitable for the $\mathrm{Ni}(14\,\mathrm{nm})/\mathrm{CaF}_2$ sample:

- Thickness of ferromagnetic layer $t = 14$ nm

- Effective magnetization $M_{\mathrm{eff}} = 195 \pm 16$ kA/m

- Gyromagnetic ratio $\gamma/2\pi = 33.4$ GHz/T

- Continuum exchange constant $\alpha_{\mathrm{ex}} = 5 \cdot 10^{-17}$ m^2 ($\alpha_{\mathrm{ex}} = 2A/\mu_0 M_{\mathrm{sat}}^2$, where $A = 8$ pJ/m is the exchange constant for Ni, see e.g. [34])

- Resonance magnetic field $\mu_0 H_{\mathrm{res}}$: experimental values reported in Fig.5b of the main text; uncertainty is $\pm 5\%$

- Angle between wavevector and magnetic field $\varphi = 15°$

In Fig.S6 we show the results of the SW dispersion calculations. Blue band is related to RSAW-driven SWs, red band is related to SSLW-driven SWs. For both, the finite width of the semi-transparent ribbon represents the combination of error in M_{eff} and $\mu_0 H_{\mathrm{res}}$; the solid line is the calculation based on the most-likely parameters. As expected, the SW band vertically shifts upon application of a magnetic field; its non-monotonicity cannot really be appreciated on the plotted scale. Note that in our experimental conditions the critical angle θ_{DE} for the appearance of the Damon-Eshbach mode is between 7° and 17° (depending again on the applied magnetic field, see [53]). Thus, at $\varphi = 15°$ we are exciting a mixture of BVMSW and DE. We are probably not able to resolve the two modes since close to θ_{DE} the DE mode i) is almost degenerate to BVMSW and ii) has a large damping.

In Fig.S6, superimposed to the dispersion bands, the experimental data (see Fig.5b of the main text) are shown as white dots with frequency error bars (the wavevector error bars are within the marker size). Good agreement between experimental data and computed dispersions is found. This should not impress, since the dispersions are computed on the basis of the parameters obtained from the experimental data themselves.

What matters here is that from these calculations it is possible to quantify the curvature of the dispersions. In the plotted frequency-wavevector region the bands are basically flat. We can roughly quantify the flatness F as

$$F = \frac{\nu(q = q_{\text{exp}}) - \nu(q = 0)}{\nu(q = q_{\text{exp}})} \ , \tag{S8}$$

where ν is the computed frequency and q_{exp} is the wavevector of each experimental datum. F quantifies the relative error if the experimental data (which are at finite wavevector) are treated as if they were at zero wavevector. We obtain $F < 0.06$. Thus, we at most introduced a 6% error in analyzing our SAW-FMR data with a standard Kittel relation (see Eq.6 of the main text), which is supposed to be applied only to uniform precession data like standard FMR.
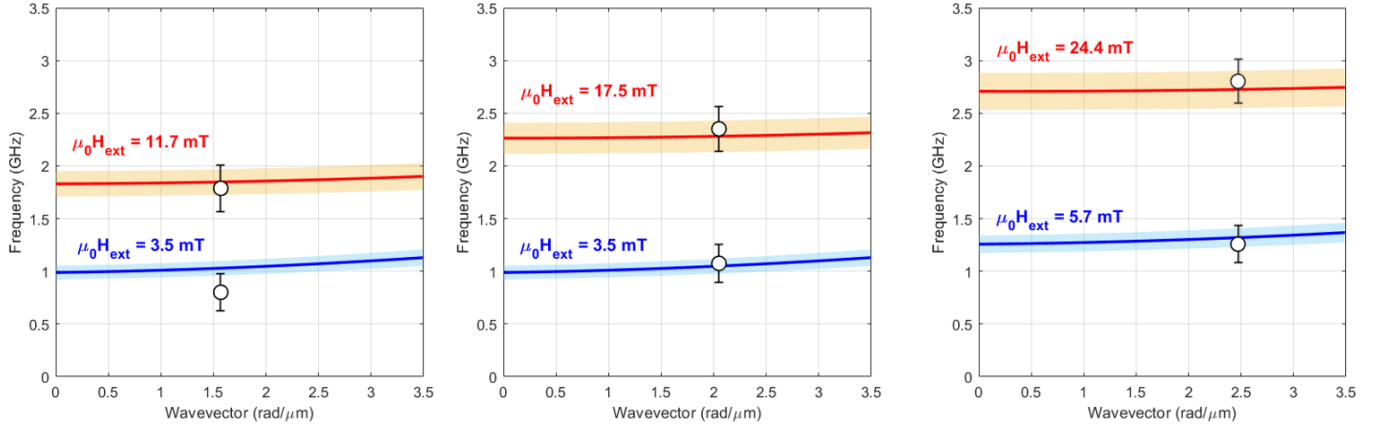

Figure S6. SW dispersions and Ni(14 nm)/CaF$_2$ experimental data. Red: SSLW-driven resonances; blue: RSAW-driven bands; solid lines are the SW dispersion based on the most-likely parameters; semi-transparent ribbons are the tolerance region considering the uncertainty on M_{eff} and $\mu_0 H_{\text{res}}$. White dots are the experimental data. Left: $q = 1.57$ rad/μm; center: $q = 2.05$ rad/μm; right: $q = 2.47$ rad/μm.

[12] H.J. Eichler, P. Günter, and D.W. Pohl, Laser-induced dynamic gratings, Springer-Verlag, 1986.

[34] J.M.D. Coey, Magnetism and magnetic materials, Cambridge University Press, 2010.

[53] C.E. Patton, Magnetic excitations in solids, Phys. Rep. 103, 251 (1984).

[54] B.A. Kalinikos, Spectrum and linear excitation of spin waves in ferromagnetic films, Sov. Phys. J. 24, 718 (1981).